Surface heat loss and chemical kinetic response in deflagration-to-detonation transition in microchannels

Wenhu Han,[1,2,*] Jin Huang,[1,†] Gongtian Gu,[1] Cheng Wang,[1] and Chung K. Law[3]
[1]*State Key Laboratory of Explosion Science and Technology, Beijing Institute of Technology, Beijing 100081, China*
[2]*School of Engineering, University of Warwick, Coventry, CV4 7AL, United Kingdom*
[3]*Department of Mechanical and Aerospace Engineering, Princeton University, Princeton, New Jersey 08544, USA*

(Received 24 January 2020; accepted 22 April 2020; published 21 May 2020)

The effects of cold, hot, and adiabatic walls on flame propagation and deflagration-to-detonation transition (DDT) in a microscale channel are investigated by high-resolution numerical simulation. Results show that the conducting, cold, and hot walls lower the flame acceleration rate, while DDT can occur and originate from local explosion near the flame tip for both the hot and adiabatic walls. Furthermore, for the adiabatic wall, autoignition near the wall produces fast flames in the boundary layer, inducing two shocks propagating and colliding at the center, inducing a local explosion near the flame tip. However, for the hot wall, fast flames do not appear in the boundary layer due to heat loss at the wall; DDT occurs due to coupling of the compression waves with the stretched flame, and needs strong local explosion due to the absence of autoignition in the boundary layer. Nevertheless, compared with the adiabatic wall, occurrence of DDT is delayed while the run-up distance is reduced because of heat input from the hot wall to the fresh gas. For the cold wall, a flame propagates oscillatorily and fails to develop to detonation. It is identified that the flame retreat is caused by thermal contraction due to heat loss at the cold wall. It is further demonstrated that realistic chemistry is needed for an accurate description of the occurrence of autoignition within the boundary layer and DDT.

DOI: 10.1103/PhysRevFluids.5.053201

I. INTRODUCTION

Flame propagation and deflagration-to-detonation transition (DDT) in micro- and mesochannels depend strongly on the channel width [1–3] through the wall conditions such as friction and heat loss. For example, while turbulent flame acceleration and the reactivity gradient mechanism have been shown experimentally to be the main causes for DDT in macrochannels (∼10 mm or greater) [4,5], studies on mesochannels have shown that the channel width affects the flame propagation characteristics, the run-up distance, the mechanism of DDT [6–8], and the detonation mode [9]. Kuznetsov *et al.* [10,11] evaluated limits for effective flame acceleration in hydrogen mixtures, and found different flame modes including slow flame, fast flame, and quasidetonation. Furthermore, as the channel width is reduced to the microscale (∼1 mm), it has been demonstrated that heat transfer and viscous friction at the wall would become important for flame acceleration and DDT [12,13]. Akkerman *et al.* [14] further showed that flame interaction with the wall can lead to oscillation of the flame propagation velocity due to variations of the shape of the curved flame, while Liberman

*hanwenhu@bit.edu.cn
†huangjin@bit.edu.cn

et al. [15] identified the possible role of the Darrieus–Landau instabilities on DDT in a narrow channel, and substantiated the theoretical result of the importance of hydraulic resistance on DDT [16] and the detonation velocity deficit [17]. The importance of hydraulic resistance in DDT in thin, semi-infinite, and thermally insulated channels was also discussed in Kagan and Sivashinsky [18,19]. Han *et al.* [20,21] further considered viscous effects on flame acceleration and DDT in a microchannel, and found that while viscosity facilitates flame acceleration, it nevertheless leads to a deficit of the detonation velocity [22,23].

While many of the above studies have considered the essential role of wall friction on detonation initiation and propagation, cursory studies have indicated the equally important role of wall heat transfer, particularly in microchannels [24]. For example, Ju and Law [25] showed that both drag and heat loss could lead to reduction of the detonation velocity. Furthermore, Ott *et al.* [26,27] numerically observed a "jerky" motion of the flame front in microchannels with isothermal walls, in which the flame runs and pauses as it propagates, while Wu and Wang [28] experimentally observed oscillating flames at low equivalence ratios for ethylene-oxygen DDT in a capillary channel.

Recognizing the potential importance of wall heat transfer on detonation propagation and DDT, we have performed a systematic computational study on detonation propagation in microchannels, with either an adiabatic wall or heat-conducting walls of various intensities, and shall demonstrate the essential role of wall heat transfer in the DDT.

In the present study we have also found it essential to consider the role of chemistry in the DDT. Specifically, it is noted that extensive studies on DDT [29] using the one-step reaction model have shown that turbulent flames create hot spots in the flame front that lead to the transition to detonation through the Zeldovich gradient mechanism [30,31], and consequently suggested that the occurrence of DDT is due to the reaction in the region between the precursor shock and the flame front. However, high-resolution simulations using detailed reaction models [32–34] instead showed that the temperature in the compressed fresh gas in front of the flame is not sufficiently high to initiate exothermic reaction on the timescales of the entire process. Indeed, it was further shown that the spatial scales of the temperature nonuniformity that is capable of initiating detonation via the Zeldovich gradient mechanism are much greater than those in hot spots or between the precursor shock and the flame front, based on one-step reaction [35,36]. Wang and Liberman *et al.* [37] recently studied the influence of chemical kinetics on detonation initiation by temperature gradients in methane-air mixtures, and showed that accurate predictions for DDT in a temperature gradient requires using detailed reaction mechanisms.

Recognizing the overwhelming evidence on the essential role of chemical kinetics in the description of the detailed structure and propagation of reaction fronts, beyond the one-step model, it behooves us to use detailed mechanisms in our study. To facilitate the study, we have used the hydrogen-oxygen system whose reaction mechanism not only is relatively simple as compared to those for hydrocarbon oxidation, it is also kinetically sharp to yield unambiguous yet interesting information enriching the study.

In the following sections we shall sequentially present the governing equations and the physical models, followed by the simulation results on adiabatic and heat-conducting walls.

II. GOVERNING EQUATIONS

The compressible and reactive flow Navier-Stokes (NS) equations, with advection, diffusion, and reaction sources, are given by

$$\frac{\partial(\rho)}{\partial t} + \frac{\partial \rho u}{\partial x} + \frac{\partial \rho v}{\partial y} = 0, \tag{1}$$

$$\frac{\partial \rho u}{\partial t} + \frac{\partial \rho u^2 + p}{\partial x} + \frac{\partial \rho u v}{\partial y} = \frac{\partial}{\partial x}\mu u\left(\frac{4}{3}\frac{\partial u}{\partial x} - \frac{2}{3}\frac{\partial v}{\partial y}\right) + \frac{\partial}{\partial y}\mu v\left(\frac{\partial u}{\partial y} + \frac{\partial v}{\partial x}\right), \tag{2}$$

$$\frac{\partial \rho v}{\partial t} + \frac{\partial \rho u v}{\partial x} + \frac{\partial \rho v^2 + p}{\partial y} = \frac{\partial}{\partial x}\mu u\left(\frac{\partial u}{\partial y} + \frac{\partial v}{\partial x}\right) + \frac{\partial}{\partial y}\mu v\left(\frac{4}{3}\mu\frac{\partial v}{\partial y} - \frac{2}{3}\frac{\partial u}{\partial x}\right), \tag{3}$$

$$\frac{\partial \rho E}{\partial t}+\frac{\partial \rho u(E+p)}{\partial x}+\frac{\partial \rho v(E+p)}{\partial y}=\frac{\partial}{\partial x}\left[\mu u\left(\frac{4}{3}\frac{\partial u}{\partial x}-\frac{2}{3}\frac{\partial v}{\partial y}\right)+\frac{\partial}{\partial y}\mu v\left(\frac{\partial u}{\partial y}+\frac{\partial v}{\partial x}\right)\right]+\frac{\partial}{\partial x}\left[\mu u\left(\frac{\partial u}{\partial y}+\frac{\partial v}{\partial x}\right)+\frac{\partial}{\partial y}\mu v\left(\frac{4}{3}\frac{\partial v}{\partial y}-\frac{2}{3}\frac{\partial u}{\partial x}\right)\right]+\frac{\partial}{\partial x}\left[\kappa\frac{\partial T}{\partial x}\right]+\frac{\partial}{\partial y}\left[\kappa\frac{\partial T}{\partial y}\right]+\sum_{k=1}^{N}\frac{h_k}{M_k}\left[\frac{\partial}{\partial x}\left(\rho D_k\frac{\partial Y_k}{\partial x}\right)+\frac{\partial}{\partial y}\left(\rho D_k\frac{\partial Y_k}{\partial y}\right)\right], \tag{4}$$

$$\frac{\partial(\rho Y_i)}{\partial t}+\frac{\partial \rho u Y_i}{\partial x}+\frac{\partial \rho v Y_i}{\partial y}=\frac{\partial}{\partial x}\rho D_i\frac{\partial Y_i}{\partial x}+\frac{\partial}{\partial y}\rho D_i\frac{\partial Y_i}{\partial y}+\dot{\omega}_i, \tag{5}$$

$$E=h+\frac{p}{\rho}+\frac{u^2}{2}, \tag{6}$$

$$p=\sum_{i=1}^{N}\rho Y_i R_i T=\rho\left(\sum_{i=1}^{N}Y_i R_i\right)T \quad R_i=\frac{R_u}{W_i}, \tag{7}$$

$$h=\sum_{i=1}^{N}Y_i h_i, \tag{8}$$

$$h_i(T)=h_i^f+\int_{T_0}^{T}c_{p,i}(\hat{T})d\hat{T}, \tag{9}$$

where p, ρ, T, u, E, and h are pressure, density, temperature, x velocities, and total energy and enthalpy per unit mass; Y_i the mass fractions of species i with $\sum_{i=1}^{N}Y_i=1$; M_i, R_i, c_{pi}, h_i^f, and D_i are the molecular weight, specific gas constant, specific heat, the enthalpy of formation, and the diffusion coefficient of species i; $R_u=8.31\,\mathrm{J/(mol\,K)}$ the universal gas constant, and μ and κ the dynamic viscosity and thermal conductivity of the mixture, respectively. The mixture properties are evaluated using the CHEMKIN [38] and TRANSPORT [39] packages, in which the mixture-averaged transport model is used to determine the mixture-averaged species diffusion coefficients and a mole-fraction-based model is used for the diffusion velocity. Hence, we transfer the mass fraction to mole fraction for the diffusion coefficient obtained in the CHEMKIN and TRANSPORT packages.

We adopt the San Diego mechanism [40] which comprises eight species: H_2, O_2, OH, O, H, H_2O, HO_2, and H_2O_2. The physical flux is split by the weighted essentially nonoscillatory Lax-Friedrichs (WENO-LF) method [41,42] and the spatial discretization of the advection and diffusion terms by the fifth-order WENO and sixth-order central difference schemes. To solve the stiffness problem, an explicit-implicit additive Runge-Kutta scheme [43] was used in the time discretization. The Courant-Friedrichs-Lewy number is 0.2 in the simulations.

The computational domain is a two-dimensional (2D) channel of 4×10^{-4} m width and 1.5 m length, filled with a stoichiometric H_2-O_2 mixture. A weak energy source is set at $0\leqslant x\leqslant 2\times10^{-4}$ m to ignite a planar flame, with $T=2400$ K and $\rho=\rho_0/4$. In the unreacted mixture, the initial velocity, temperature, and pressure are 0.0 m/s, 300 K, and 1 atm, respectively. The left end is closed, while the right end is nonreflective. Both the upper and lower boundaries are described by nonslip walls with adiabatic and heat-loss boundary conditions. The thermal loss at the left and right ends is neglected because the channel is very narrow. For the adiabatic wall, we have $\partial T/\partial y=0$. For the conducting wall, we have $\partial T/\partial y=-\mathrm{Bi}(T-T_0)$, where T_0 is the wall temperature and Bi the Biot number denoting the normalized heat loss, and is set at a fixed $\mathrm{Bi}=2$. We study three cases of wall condition, namely, the adiabatic wall, the cold wall at $T_0=300$ K, and the hot wall at $T_0=600$ K [18,24].

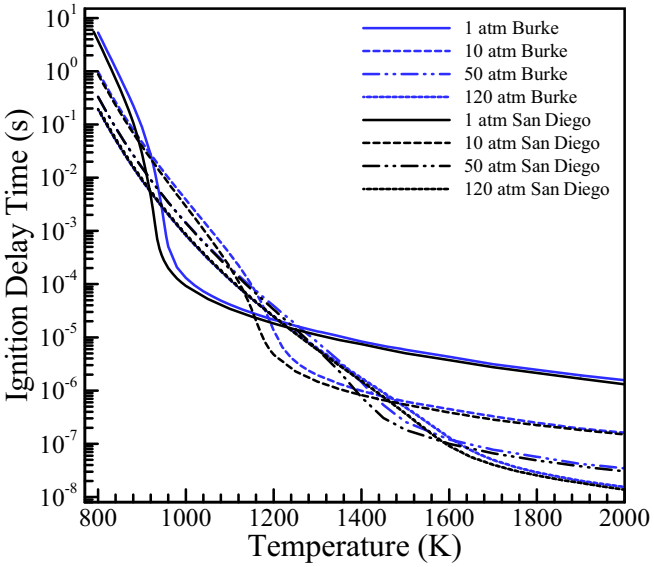

FIG. 1. Ignition delay time as a function of temperature for H_2-O_2 system with the developed San Diego mechanism [40] and Burke's mechanism [44–46].

III. RESULTS AND DISCUSSIONS

A. Verification of reaction mechanism

Figure 1 shows the ignition delay time as a function of temperature for different pressures. It is seen that the ignition delay time shows the crossover behavior; namely, at certain temperature, the ignition delay time suddenly drops, which is mainly due to the second limit for H_2-O_2 mixtures. When the temperature reaches this value, the kinetic time becomes much faster as it crosses the boundary from the slow reacting regime controlled by the HO_2 kinetics to the fast reacting regime controlled by the $H + O_2$ chain branching. Increasing pressure reduces the ignition delay time substantially, while the crossover behavior becomes less prominent and increases significantly, with 900, 1200, 1500, and 1650 K for 1, 10, 50, and 120 atm, respectively. The validation of the present reaction mechanism is verified by calculating the ignition delay time with the Burke and the San Diego mechanisms. Results demonstrate that the ignition delay times calculated by these two mechanisms agree closely except for minor differences in the crossover temperatures. We have therefore adopted the San Diego mechanism in the simulation over a wide range of pressures.

B. DDT for different wall conditions

Figure 2 shows the position of the flame tip and the propagation speed as functions of time for different wall conditions, demonstrating that wall heat loss can cause significant difference in the flame acceleration and DDT. Specifically, for the adiabatic case, a laminar flame accelerates steadily and eventually transitions to a detonation, at which the propagation speed jumps to ~3800 m/s at $t \sim 80 \times 10^{-6}$ s as an overdriven detonation, and then decays to a value below the Chapman-Jouguet (CJ) state. For the hot wall, the flame acceleration rate is lowered due to heat loss. Nevertheless, DDT still develops except it takes longer, occurring at $t \sim 100 \times 10^{-6}$ s, with the formation of a strong overdriven wave with the velocity of ~4200 m/s. It is of interest to note that the run-up distance of DDT in the hot-wall case is slightly shorter than that of the adiabatic case. This is because the heat input from the hot wall to the unreacted gas in front of the flame facilitates reactions upstream. As the wall temperature is 300 K, the flame initially accelerates and propagates slower

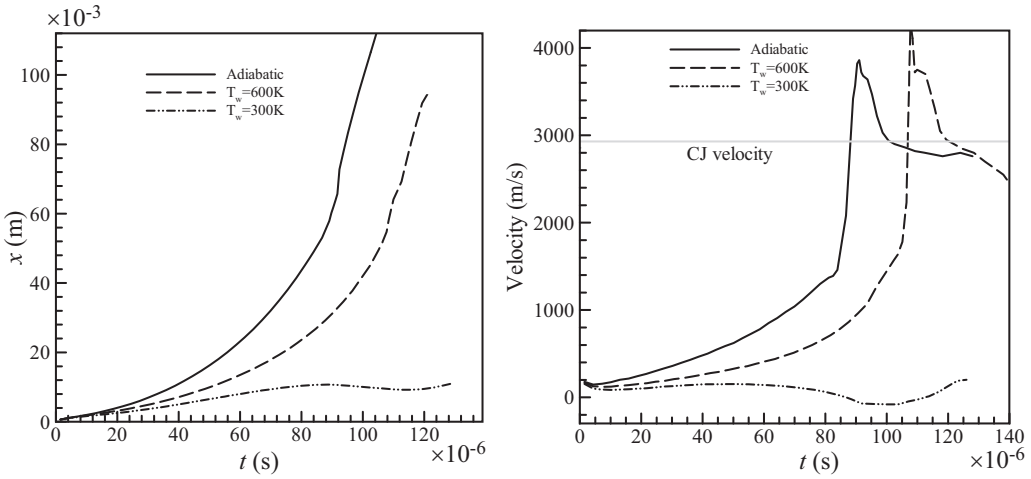

FIG. 2. Flame-tip position and velocity as a function of time.

as compared to the hot-wall case. It subsequently decelerates and retreats, with a negative velocity, such that an oscillating flame eventually develops and cannot transition to a detonation.

In the microchannel, evolution of the flame front throughout the entire DDT process is shown in Fig. 3. The flame is stretched due to viscous drag at the walls, leading to an increase in its surface area, and accelerates as a consequence. The acceleration generates compression waves that preheat the unburned gas in front of the flame, leading to further flame acceleration which in turn strengthens the compression waves. This positive feedback through superposition of the compression waves then leads to the formation of the precursor shock, and hence attainment of the DDT in the present adiabatic case. For the hot-wall case, Fig. 2 shows that DDT occurs at $t \sim 110\,\mu$s. Evolution of the global flame is similar to that in the adiabatic case, shown in Fig. 3(b), and the flame shapes are similar. The process of transition to detonations is discussed later in more detail.

Figure 4 shows that the gas ahead of the flame is compressed and preheated substantially so that a temperature gradient is formed between the flame front and the shock. It is seen that the

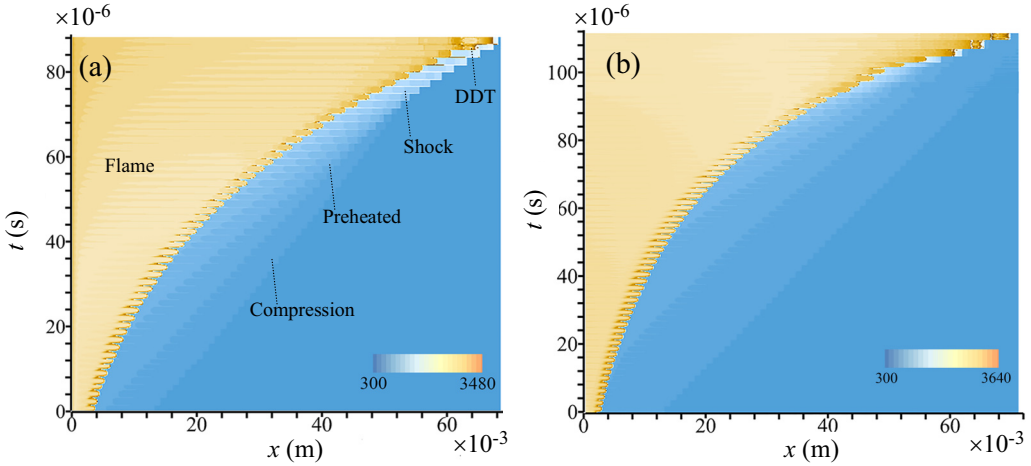

FIG. 3. Entire process of flame acceleration and DDT: (a) adiabatic wall; (b) hot wall.

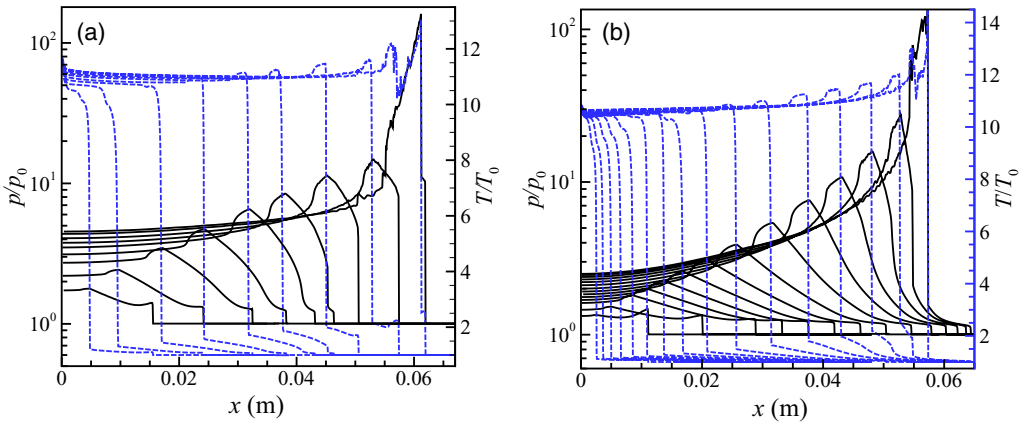

FIG. 4. Temperature and pressure profiles during DDT: (a) adiabatic wall, $t = 23.18$, 37.49, 51.91, 61.50, 69.85, 75.68, 80.84, 86.76, and 89.68 μs; (b) hot wall, $t = 15.98$, 30.91, 45.19, 53.29, 61.14, 68.78, 75.88, 83.3, 91.0, 96.52, 101.07, 104.57, 107.27, and 108.37 μs.

temperature of the products behind the flame front is lower for the hot wall than that in the adiabatic case due to heat loss at the walls. The compression wave produced by the ignition source compresses and preheats the gas ahead of the flame, which promotes growth of the leading shock created by the accelerated flame. For the hot-wall condition, growth of the leading shock induced by the accelerated flame is slower due to heat loss, compared with that with adiabatic conditions. As the flame advances, the temperature of the preheated gas at the center increases to ~700 K, while the temperature near the wall is constrained by the constant wall temperature, which is lower than that in the adiabatic case due to heat loss. Consequently, autoignition does not occur near the wall, although viscous heating elevates the temperature in the boundary layer. However, as the flame accelerates, the precursor shock strengthens continuously and increases the temperature upstream. A compressed and preheated zone is formed between the precursor shock and flame fronts. Due to compression waves induced in the zone, the temperature near the flame tip increases further and a temperature gradient forms between the flame front and the leading shock. At $t = 107.27\,\mu$s the temperature and pressure near the flame tip are ~700 K and ~18.2 atm, respectively, under which the ignition delay time is $\sim 1.8 \times 10^{-8}$ s. Consequently, autoignition near the flame tip develops rapidly and triggers local explosion, leading to DDT.

C. Flame frontal structure and DDT

1. Adiabatic wall and hot wall ($T_0 = 600$ K)

In the initial stage of flame propagation, the typical flame structure including the reactivity information at $t = 16.01\,\mu$s is shown in Fig. 5. It is seen that the flame is extended and takes a finger shape. The species mass fractions show that HO_2 and H_2O_2 apppear early and are primarily distributed at the flame front, followed by H and OH, leading to the major chain-branching reactions and eventually ignition. This implies as expected that the emergence of HO_2 is also the indication of the initiation of the reaction zone for the ignition reactions. Furthermore, the HO_2 mass fraction is $\sim 10^{-3}$ and the H_2O_2 mass fraction is at a lower order than that of HO_2 as intial pressure is low, ~1 atm.

The above observation is further corroborated in the lower panel of Fig. 5, which shows the species mass fractions along the center and the wall of the channel. It is seen that the peaks of the mass fractions of HO_2 and H_2O_2 are, respectively, 2×10^{-3} and 2.5×10^{-4}. They are subsequently

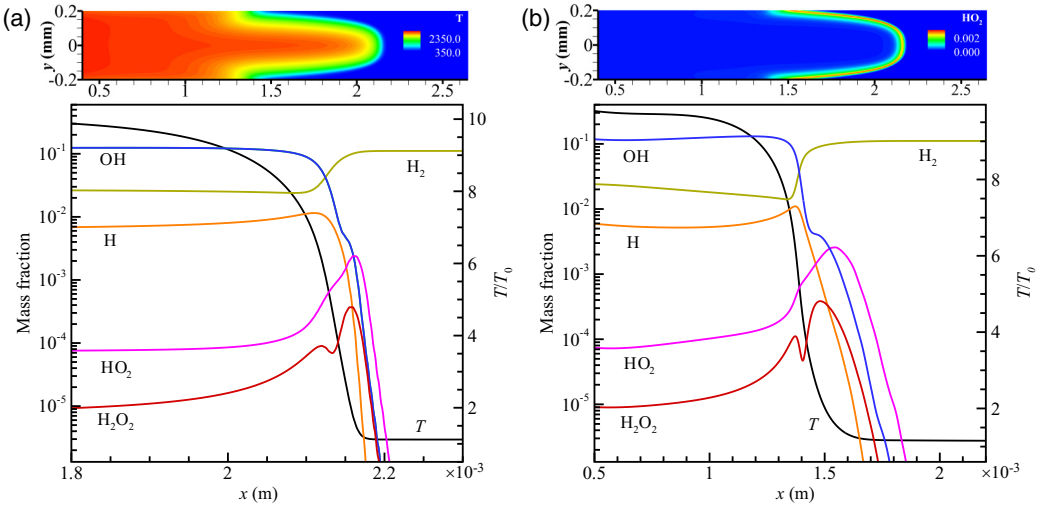

FIG. 5. Temperature and mass fraction profiles of species (a) at center and (b) near wall at $t = 16.01 \times 10^{-6}$ s for the adiabatic wall.

consumed rapidly, with the concomitant generation of OH and H and hence progression of the chain-branching reactions, leading to increased temperature. It is also noted that there is a hump following the peak in the H_2O_2 mass fraction profile. Consequently, the active reaction zone, which approximately spans between 2.0 and 2.2 cm, can be considered to consist of two layers, namely, a leading, H consumption layer, followed by an H production layer. The H consumption layer coincides with the concentration profile of HO_2, which is the first noticeable radical as the free-stream mixture enters the active reaction zone of the flame. Initiation is through the back diffusion of H which reacts with O_2 through the branching reaction $H + O_2 \rightarrow OH + O$. The above structure therefore conformsto that of a premixed flame [47], as expected.

As the flame elongates steadily, its length reaches ~1.65 mm at $t = 86.7 \times 10^{-6}$ s, as shown in Fig. 6. The compressed and preheated zone is produced by precursor shock. The barrage of acoustic waves is compressing the unburned material in the zone, shown in Fig. 9. As the flame goes into the zone with the barrage of acoustic waves small skirts appear at its surface, with a small cusp at the tip. At the skirts, OH, H, HO_2, and H_2O_2 mass fractions are locally higher, demonstrating that the disturbance can enhance locally the reaction rate and heat release at the flame front. Consequently, the interaction of the acoustic wave with the reactions affects the flame. Nevertheless, since the flow is still laminar in the microchannel, the disturbance is not amplified and the flame does not develop into a turbulent one. Furthermore, the positive feedback between the flame front and the shock can increase the heat release rate and further accelerate the flame. Due to the compression wave, the pressure and temperature at the tip of the flame is ~14.6 atm and ~630 K, while the temperature near the wall is ~685 K due to viscous friciton. At this instant, the flame thickness at the flame tip is $\sim 8.2 \times 10^{-5}$ m and the present grid resolution can guarantee ~80 points per flame thickness, which is sufficient to capture the combustion characteristics.

As the pressure and temperature increase, the important reactions involving H, OH, HO_2, and H_2O_2 change. The HO_2 mass fraction is now higher than that of H at the front, demonstrating that HO_2 becomes more important for ignition of the gas entering the front, shown in the lower panel of Fig. 7. Species mass fractions near the wall exhibit small fluctuations, while those along the center are relatively smooth, demonstrating that the interaction of the acoustic wave with the boundary is stronger. Comparing Figs. 5 and 6, it is seen that at the front the H mass fraction is lower, while the HO_2 mass faction increases from its initial value. This is reasonable because reactions involving HO_2 are related to pressure, and generally HO_2 becomes progressively more

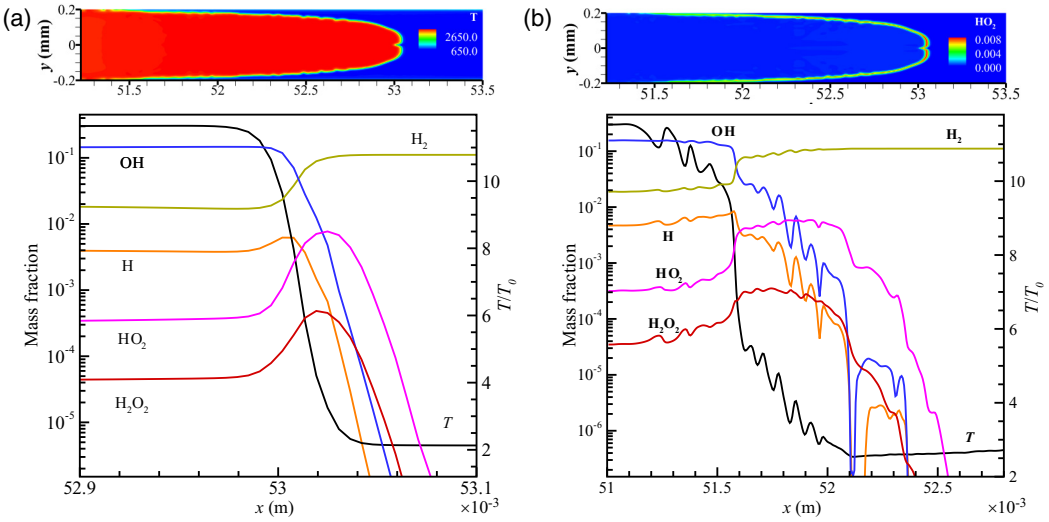

FIG. 6. Temperature and mass fraction profiles of species (a) at center and (b) near wall at $t = 86.7 \times 10^{-6}$ s for the adiabatic wall.

important with increasing pressure; the hump in the H_2O_2 mass fraction profile disappears, and the HO_2 and H_2O_2 mass fractions are higher at the flame tip. This is important for the occurrence of DDT in the adiabatic case.

Furthermore, typical profiles of the species reaction rates in Fig. 7 also show that the reaction rate of HO_2 becomes larger than that of H as pressure increases, substantiating that reactions involving HO_2 constitute the main pathway to ignition in the flame structure. In the detonation structure, consumption of HO_2 leads to the increase of H_2O_2 concentration through $HO_2 + HO_2 \rightarrow H_2O_2 + O_2$, with the corresponding reaction rates increasing significantly. Consequently, this substantiates that while reactions related to H are important, reactions involving HO_2 at high pressure also are critical, and reactions of H_2O_2 play a considerable role in the formation of DDT.

At the hot-wall boundary, the temperature of the preheated gas ahead of the flame front is ~700 K at the center and ~900 K near the wall (Fig. 8), which is higher than those (at $x \sim 5.31 \times 10^{-2}$ m) of the adiabatic wall, while the flame is also thicker, being $\sim 7.2 \times 10^{-5}$ m. This is reasonable because during the substantial period of flame acceleration, the gas ahead of the flame is heated by the hot wall to almost close to the state of transition to detonation. At the flame front, it is seen that the peaks of the mass fractions of H, HO_2, and H_2O_2 are 4×10^{-3}, 4×10^{-3}, and 5×10^{-4}, respectively, while the maximum OH mass fraction is 8×10^{-2}. Furthermore, H, HO_2, and H_2O_2 are consumed in the high-temperature regime, while the OH mass fraction increases to 1.1×10^{-1}, demonstrating that high-temperature reactions are mainly through $H + O_2 \rightarrow OH + O$ and

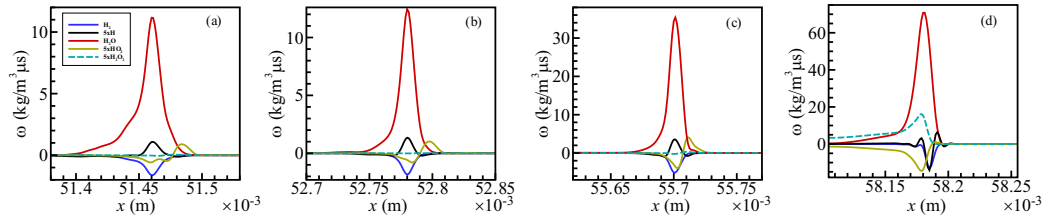

FIG. 7. Reaction rate of critical species at center for the adiabatic wall: (a) 85.72 μs, (b) 86.61 μs, (c) 88.34 μs, and (d) 89.12 μs.

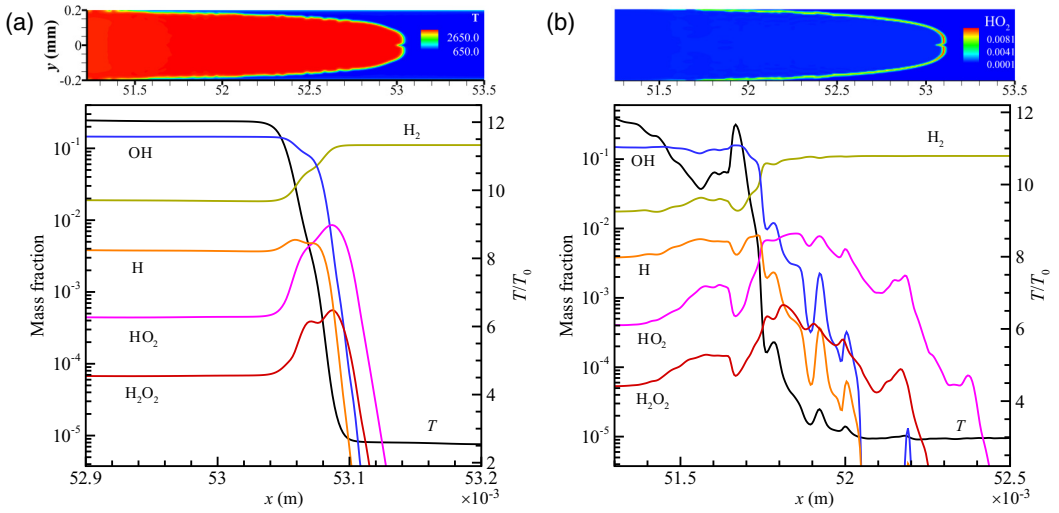

FIG. 8. Temperature and species mass fraction profiles at (a) center and (b) near wall at $t = 107.5\,\mu$s for the hot wall.

$O + H + M \rightarrow OH + M$. Strong fluctuations are also present over the temperature and species mass fraction profiles near the wall due to the interaction of the hot wall with acoustic disturbance.

As the flame accelerates steadily, the precursor compression waves strengthen and elevate the temperature ahead of them, leading to a significant reduction of the ignition delay time in the compressed and preheated gas. When the flame propagates into the fresh gas, DDT can be triggered, as indicated in Fig. 3. In the process of DDT, Fig. 9 shows evolution of the frontal structure to reveal in detail the DDT mechanism and its dependence on the chemistry. It is seen from Fig. 9(a) that at $t = 88.87\,\mu$s, a local explosion occurs and develops forward to an overdriven detonation, with two shock waves propagating oppositely. Eventually, the forward-running explosion wave evolves into a cellular detonation and triple points are developed over the detonation front, with long transverse waves behind the front at $t = 89.14 - 89.17\,\mu$s. Furthermore, autoignition in front of the flame first occurs near the wall due to friction caused by the interaction of the leading shock with the boundary layers, and rapidly develops to a fast flame propagating along the boundary layer. This was also observed in Houim *et al.* [48] and Dzieminska and Hayashi [49] using the detailed reaction mechanism. The fast flames propagate at an average speed of ~950 m/s and produce two strong shocks propagating toward the center. At $t = 88.77\,\mu$s, the two shocks collide with each other, and further compress and preheat the unreacted gas between the fast flames. In particular, the gas near the tip of the flame has a higher temperature due to thermal diffusion from the flame. When the ignition delay time is small enough, the local heat release is amplified rapidly by the shocks through the shock wave amplification by coherent energy release mechanism and a local explosion is triggered.

The shocks induced by the fast flames run backward and form retonation I through initiating the unreacted gas near the walls, while shocks running in the opposite direction form retonation II. The explosion wave advances and evolves to a cellular detonation.

Figure 9(b) shows the detailed process of DDT for the case with the hot-wall boundary. It is seen that a local explosion occurs near the flame tip at $t = 107.77\,\mu$s, which is caused by autoignition of the gas near the flame tip. It subsequently develops to a detonation and simultaneously a retonation wave is observed, propagating oppositely and consuming the unreacted gas left behind the explosion wave. Due to heat loss at the wall, a flame is not developed in the boundary layer. Eventually, a cellular detonation forms, with transverse waves behind the front. It is noted that for the hot-wall case, formation of the local explosion differs significantly from the adiabatic case, in that there is

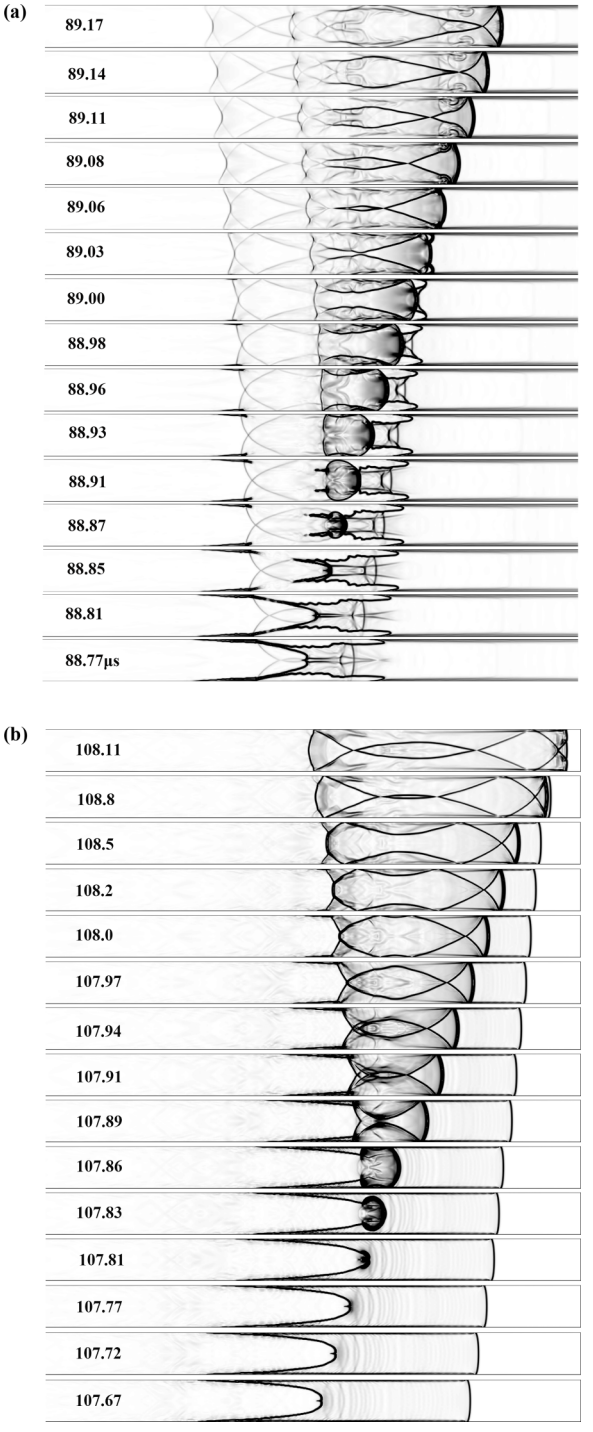

FIG. 9. DDT process (density gradient): (a) adiabatic wall; (b) hot wall.

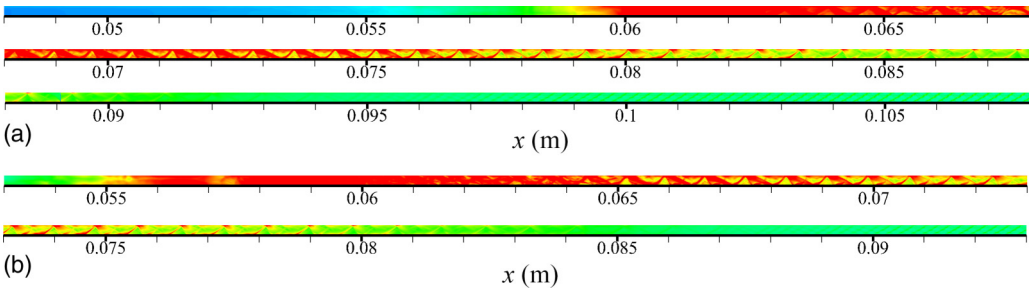

FIG. 10. Histories of maximum pressure in DDT and detonation propagation: (a) adiabatic wall; (b) hot wall.

neither autoignition near the wall nor fast flame in the boundary layer because of heat loss at the wall. For the adiabatic case, the occurrence of a local explosion is facilitated due to the appearance of the fast flame in the boundary layer, so that the occurrence of DDT is relatively far from the precursor shock induced by the accelerating flame. However, compared with the adiabatic case, a flame for the hot wall takes a longer time to induce the stronger leading shock and then triggers a strong local explosion. Nevertheless, the run-up distance of DDT is shorter due to preheating of the unreacted gas by the wall during the flame acceleration.

After DDT, the strongly overdriven detonations decay and evolve to single-head mode. As it tends to the CJ state, the single-head mode cannot sustain and the detonation degenerates to the deflagration wave, shown in Fig. 10. For the hot wall, strongly overdriven detonation quenches faster due to heat loss, which is substantiated by the maximum pressure at the center in Fig. 10. Consequently, this demonstrates that the 0.4-mm channel can indeed accommodate the occurrence of DDT in the stoichiometric H_2-O_2 mixture, while it cannot permit self-sustaining detonation. The failure to sustain detonation is promoted due to heat loss at the walls. Taylor *et al.* [50] suggested that detailed reaction mechanisms did not capture the cell irregularity and size of a cellular H_2-air detonation because of discrepancies between simulated and measured cell patterns. Differences in cell sizes computed and measured for H_2-O_2-Ar systems could be attributed to the absence of thermodynamic nonequilibrium behind the leading shock of the detonation in the simulation. Consequently, in the present simulation the detonation structure after DDT is numerically valid, while the cell size should be less than that measured in the experiments. Although it is confirmed that the 0.4-mm channel cannot permit self-sustaining detonation in the experiments, the irregularity of the detonation structure needs to be reassessed by considering thermodynamic nonequilibrium behind the leading shock of the detonation in future works.

In summary, for the adiabatic wall, DDT originates from a local explosion in front of the flame tip, which is caused by the collision of compression waves induced by the fast flames, which in turn are produced by autoignition near the wall. This autoignition was experimentally observed in experiments in a rapid compression machine and induced a superdetonation in the combustion chamber [46]. Furthermore, the DDT does not originate from the fast flame; rather it appears at the tip of the fast flame in the present microscale channel. A local explosion in the center occurs faster than the DDT from the fast flame in the boundary layers. For the hot-wall case the transition mechanism of DDT differs significantly from that in the adiabatic case, although DDT can form for both. Compared to the adiabatic case, the occurrence of DDT requires stronger local explosion due to the absence of a fast flame in the boundary layer, as substantiated by the peak pressure in Fig. 11. Nevertheless, heat input from the hot wall is able to preheat the unreacted gas in front of the flame and consequently the run-up distance of DDT is shorter than that in the adiabatic case. Moreover, in the 0.4-mm channels with both adiabatic and hot walls, while DDT can occur, the resulting detonation fails to be sustained.

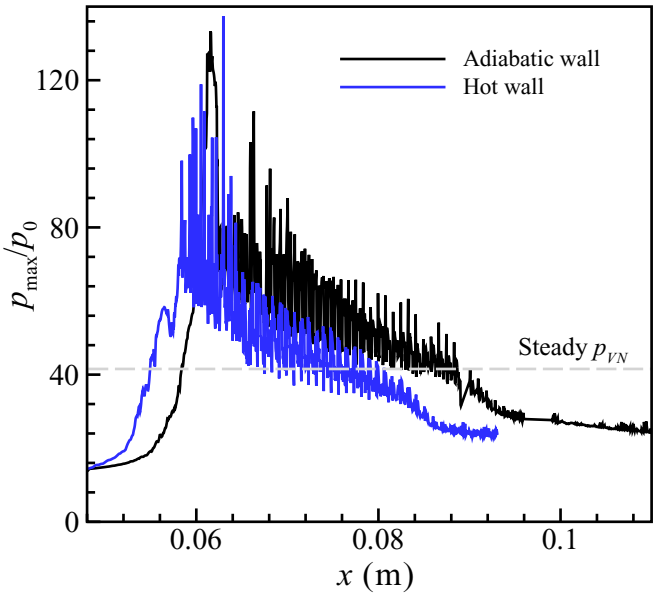

FIG. 11. Histories of maximum pressure at axis of channel in Fig. 10.

2. Cold wall ($T_0 = 300$ K)

As shown in Fig. 2, for the cold wall an oscillating flame forms and DDT is not developed. Figure 12 shows evolution of the flame structure to reveal the formation of the oscillating flame. Specifically, the flame front oscillates during $t = 1.5 - 129.1\,\mu$s, resembling the observation in Ref. [26]. Since the open end is set as a nonreflecting boundary in the simulation so that the compression waves are not reflected from the end, the backward motion of the flame front is caused by the thermal contraction induced by heat loss at the cold wall.

Mechanistically, the flame initially advances and the amount of heat loss at the wall accumulates; it then decelerates and induces expansion waves ahead of it. As a result, a backward-running flow in the upstream area is observed. Subsequently, the accumulated heat loss causes it to decelerate and then retreat, shown in Fig. 12, with the retreating flame shortening and the combustion temperature decreasing. At $t \sim 94.76 - 120.0\,\mu$s the reverse flow caused by the thermal contraction induces the reactants to enter into the flame front.

As the flame retreats and the amount of heat loss at the wall is reduced, thermal contraction weakens and the flame advances again due to friction at the wall. The oscillating motion produces the complicated flow in the vicinity of the flame front. Due to friction, the flame near the wall accelerates and its surface extends substantially. Simultaneously, the flow upstream is directed forward and the flame also propagates forward accordingly.

We next discuss evolution of the species mass fraction profiles during the oscillatory propagation. The OH mass fraction is basically consistent with the temperature distributions since OH is generated by high-temperature reactions in the flame structure. The peak of the H mass fraction is distributed uniformly at the flame front because of its low molecular weight and hence high diffusive mobility. As the flame retreats, OH and H are still present at the flame front, demonstrating that reactions still continue and the flame does not extinguish. During the flame retreat, HO_2 and H_2O_2 are retained upstream at the center and near the wall because of their relatively large molecular weight. Retaining HO_2 and H_2O_2 near the wall consequently facilitates ignition there as the flame advances again. Figure 13 shows the pressure profiles at the center and near the wall. It is seen that at $t = 94.76 - 101.06\,\mu$s, during which the flame retreats, globally an inverse pressure gradient is

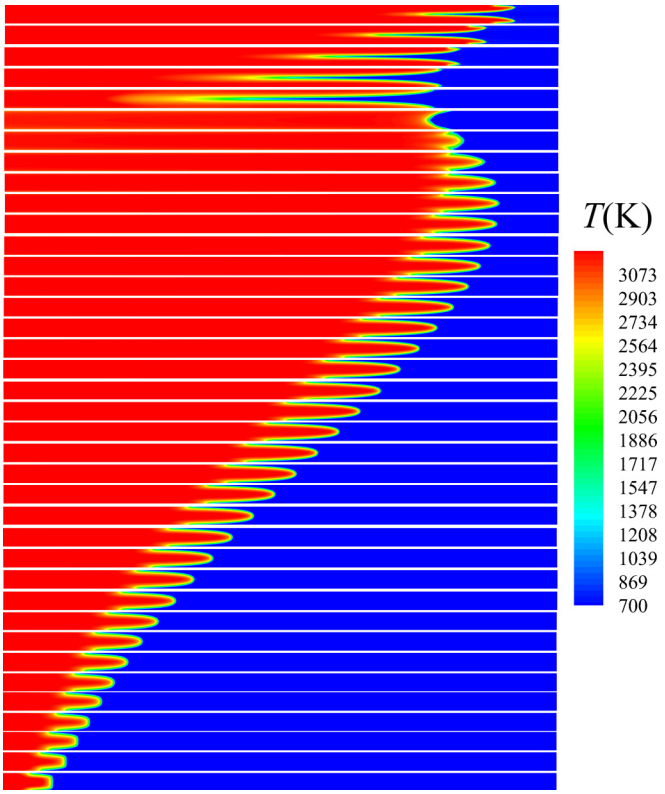

FIG. 12. Evolution of the flame front: $t = 1.5 - 129.1\,\mu$s.

present due to the expansion wave. At $t = 120.0\,\mu$s the flame propagates forward again and the pressure gradient becomes positive, which reverses the flow upstream, as shown in Fig. 13(b).

Since the flame shape is fingerlike, the profiles of the species mass fraction span a large distance and the flame thickness is ∼1 mm. As it becomes tulip shaped [15,51–53], the thickness increases to ∼5 mm. At $t = 94.76\,\mu$s, the peak of the H mass fraction is ∼0.012, and those of the OH, HO_2, and H_2O_2 mass fractions are, respectively, ∼0.11, 2.2×10^{-3}, and 4.8×10^{-4}; at $t = 120.0\,\mu$s, the peak of the H mass fraction decreases to ∼0.01 and the peaks of the OH, HO_2 mass fractions increase, respectively, to ∼0.148 and 3.4×10^{-3}, while the peak of the H_2O_2 mass fraction decreases to $\sim 3.35 \times 10^{-4}$. This indicates that in the retreating flame, reactions involving H and HO_2 are important for ignition at the cusp of the flame.

D. Comparison and discussion

Figure 14 shows the evolution of the positions of the flame surface at the center and the wall as well as the stretch length for different wall conditions, where stretch length is the distance between the flame tip and the intersection of the flame surface with the wall. It is seen that, for both the adiabatic and hot walls, the stretch length initially increases and then decreases, such that there is a maximum stretch length in the flame acceleration process. For the adiabatic wall, the maximum length is $\sim 6 \times 10^{-3}$ m at $t \sim 50\,\mu$s, while it is $\sim 2 \times 10^{-3}$ m at $t \sim 75\,\mu$s for the hot wall. Consequently, flame acceleration depends mainly on the stretch effect in the initial stage, while the positive feedback is dominant for the flame acceleration in the later stage as the compression waves are strong. The positive feedback between the advancing flame and the flame-driven precursor shock

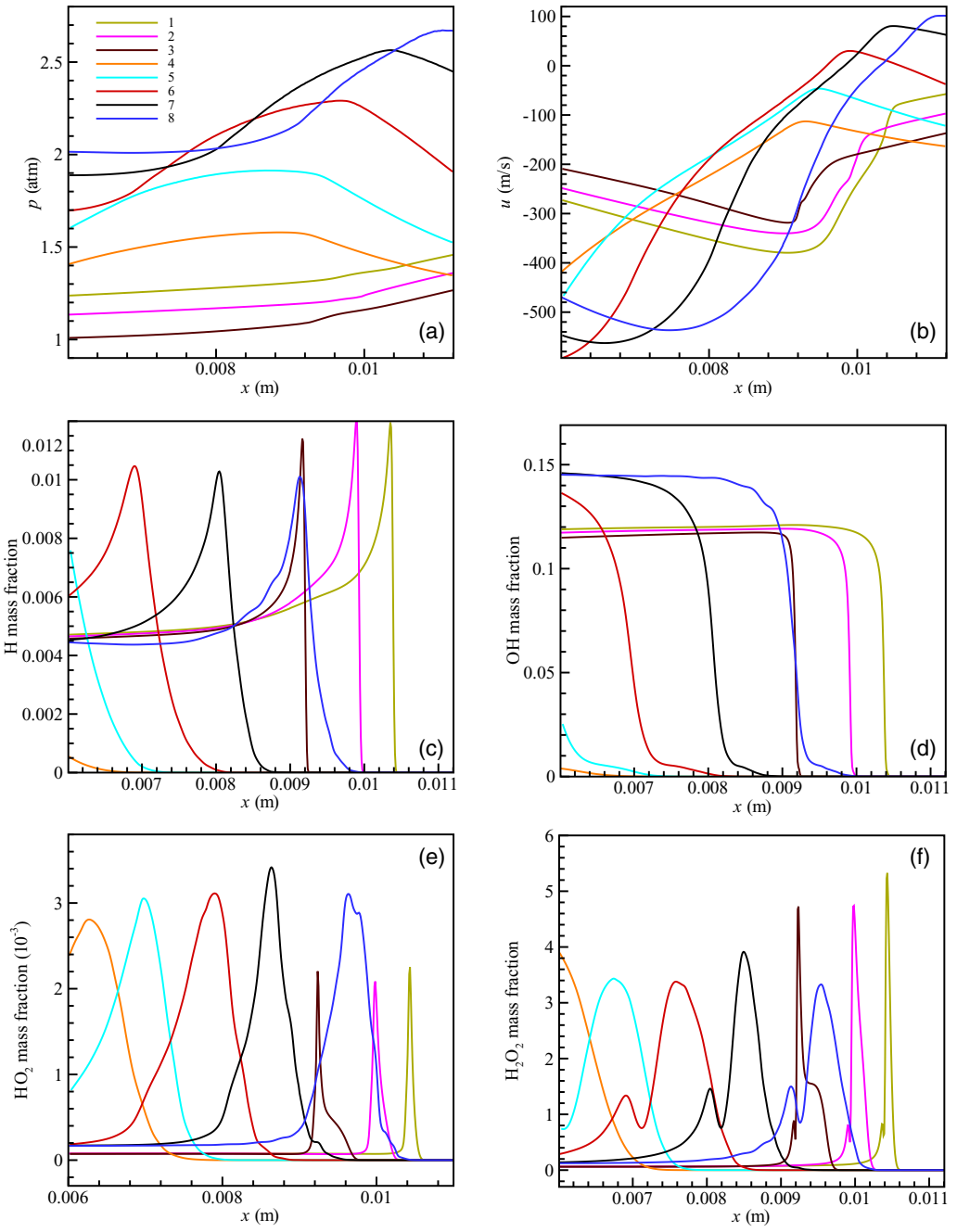

FIG. 13. Pressure, x-flow velocity, and species mass fraction profiles along the center of Fig. 12: 1–8, $t = 94.76$, 97.89, 101.06, 116.94, 120.0, 123.02, 126.03, and 129.05 μs.

is important for the subsequent flame acceleration due to heat loss at the hot wall, as compared to that in the adiabatic case. For the adiabatic wall, the flame accelerates to ~650 m/s at $t \sim 50\,\mu$s, and then reaches ~1600 m/s at $t \sim 80\,\mu$s under the positive feedback of the compression wave. However, for the hot-wall case the flame speed just reaches to ~500 m/s ($t \sim 75\,\mu$s) through stretch, while

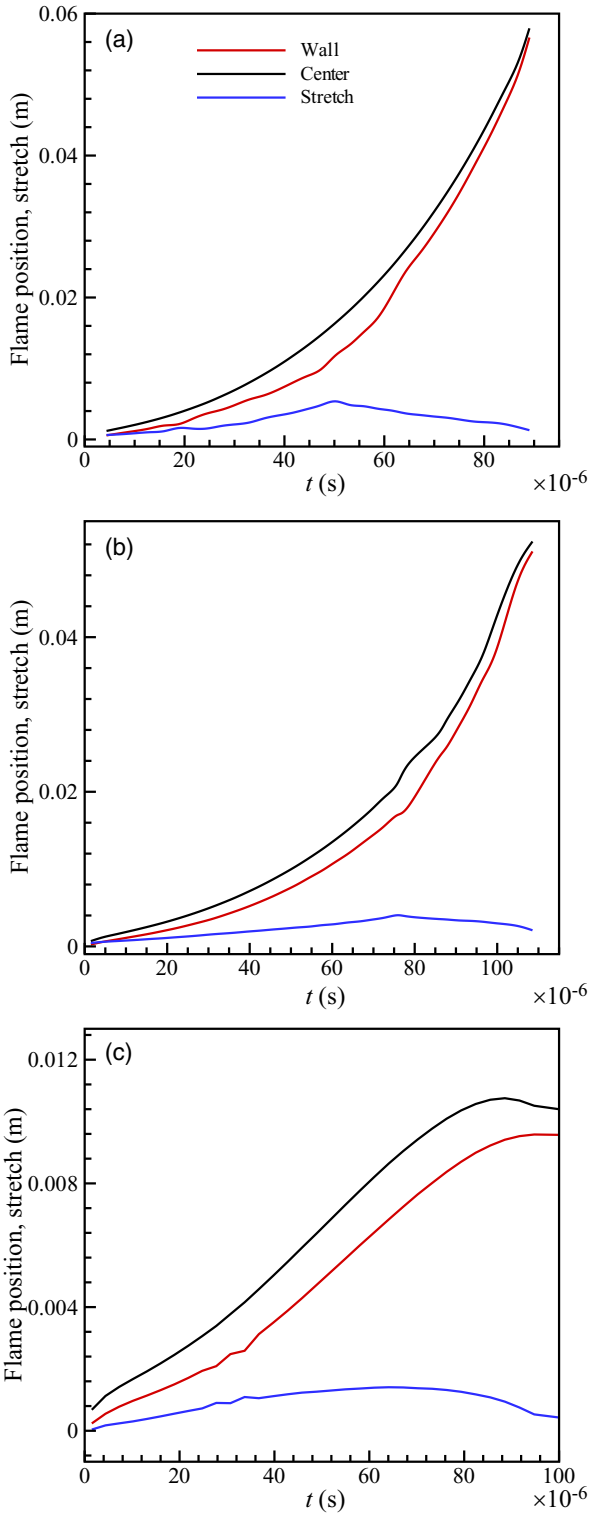

FIG. 14. Positions of the flame surface at the center and wall, as well as flame stretch versus time for cases with (a) adiabatic wall, (b) hot wall, and (c) cold wall: black (center), red (wall), blue (stretch).

the positive feedback of the compressed and preheated effect makes it up to ∼1880 m/s. However, due to the short period, the amount of heat loss is relatively small. During $t \sim 0 - 75\ \mu$s, the entire system is able to receive heat from the wall, and hence the heat stored in the unreacted gas reduces the DDT distance as compared to that of the adiabatic case.

The scenario of DDT can be classified based on the transition modes, including transition that originates at the flame front and at the shock front, and transition that originates at the contact discontinuity formed by the superposition of the pressure waves traveling in front of the flame. For a stoichiometric H_2-O_2 system, local explosion appears near the flame tip for both the adiabatic and hot walls, although the DDT modes are significantly different. In the adiabatic channel, autoignition occurs in the boundary layer in front of the flame. After the precursor shock is formed, the compression waves, which travel between the precursor shock and the flame, heat up the boundary layer once again and consequently autoignition occurs in the boundary layer. The resulting fast flame in the boundary layer induces strong shocks, the collision of which leads to local explosion appearing near the flame tip. For the hot wall, autoignition in the boundary layers is not observed, while local explosion is observed near the flame tip. This is because the precursor shock in front of the flame produced a preheated and compressed zone between the flame surface and the shock front; the latest compression wave induced by the accelerated flame propagates in the zone and shortens further the ignition delay time of the gas near the flame tip, where pressure and temperature are further enhanced. As a result, local autoignition occurs near the flame tip and leads to DDT.

For the cold wall, the maximum flame stretch length is ∼0.8 mm, which is much smaller than those of the adiabatic and hot walls; the flame speed just reaches ∼120 m/s at $t \sim 40\ \mu$s and then the length is obviously shortened. The volume contraction causes flame deceleration due to heat loss at the cold wall, which induces expansion wave and hence the reflow upstream. Due to thermal contraction, the flame retreats and then propagates forward again. The flame retreat causes the subsequent oscillatory motion of the flame front, as observed experimentally by Wu and Wang [28]. Previous studies [14,45,46] indicated that during the flame acceleration phase, an entire new volume of the gas is pushed forward in the direction of the flame propagation. However, in the present simulation, part of the product gas flows reversely due to heat loss at the wall. The burnt gas first expands at the flame front, but then the gas volume contracts and leads to the flame retreat because of heat loss to the wall. In summary, in the initial stage, the flame retreat is mainly due to accumulation of the heat loss at the wall as the flame extends. Hence, as the flame stretch decreases, it decelerates and then retreats, as shown in Figs. 12 and 14.

IV. CONCLUSIONS

Through high-resolution numerical simulations, this work examines the effects of cold, hot, and adiabatic walls on flame propagation and DDT in a microscale channel. Results show that heat loss at the wall lowers the flame acceleration rate. For the hot and adiabatic walls, a laminar flame can accelerate and transition directly to a detonation wave, while for the cold wall, an oscillating flame is generated which does not transition to DDT. For the adiabatic wall, DDT originates from a local explosion near the flame tip, which is preceded by the collision of compression waves induced by a fast flame produced by autoignition near the wall. For the hot wall, although DDT also originates from a local explosion near the flame tip, the DDT transition mechanism differs significantly from that of the adiabatic wall, in that the occurrence of DDT is delayed and the run-up distance is shorter, and it also requires a strong local explosion due to absence of autoignition in the boundary layer. For the cold wall, a flame propagates oscillatorily and cannot transition to a detonation. The flame retreat is caused by the thermal contraction induced by heat loss at the wall. Furthermore, it is shown that realistic reaction mechanism is needed to describe the interaction of shock with the boundary layer and the occurrence of autoignition.

It is also noted that the flow near the wall cannot reach thermodynamic equilibrium with the wall as the dimension is reduced to approach the mean free path of the gaseous mixture, yielding large slips of thermodynamic properties between the wall and the gas in the near-wall boundary.

There is a concentration slip across the Knudsen layer caused by the temperature jump even without species concentration gradients, and nonequilibrium effects on the temperature and concentration slips on the wall and radical quenching were studied by Xu and Ju [54]. In the microchannel, the nonequilibrium effects may influence the process of DDT. Thermodynamic nonequilibrium is not considered in the present simulation and it merits further study.

From the kinetic theory of gases, the Dufour and Soret effects are caused by second-order diffusion. However, the second-order diffusion processes are generally much smaller than the first order. The counter-gradient diffusion caused by the Soret effect in the presence of steep temperature gradients around flames for the low-molecular-weight hydrogen is very interesting. The counter-gradient diffusion around flames may influence initial flame propagation in the process of DDT, while the effect is weak as the flame accelerates due to heat expansion and flame stretch in the present simulation. In addition, the Dufour effect is usually quite small, such that it is negligible. Consequently, the Soret and Dufour effects were not considered in the present simulations. The assessment of the Soret effect in the process of DDT merits study in future works.

ACKNOWLEDGMENTS

The research of W.H. and C.W. was sponsored by the National Natural Science Foundation of China under Grants No. 11972090 and No. 11732003; the Science and Technology on Transient Impact Laboratory Foundation (Grant No. 6142606182104); and the State Key Laboratory of Explosion Science and Technology. W.H. was in addition supported by a European Commission for the Marie Curie International Fellowships Grant "TurbDDT" (Grant No. 793072).

APPENDIX: VERIFICATION OF GRID CONVERGENCE

To verify grid convergence, we used grid resolutions of 2×10^{-6} m, 1×10^{-6} m, and 5×10^{-7} m to solve the NS equations for the adiabatic case. Figure 15 shows results with different grid resolutions, demonstrating that while the solution for the lower grid resolution differs from those with the higher grid resolutions, the solutions with the 1×10^{-6} m and 5×10^{-7} m resolutions are basically consistent with each other, with only minor differences in the later stage of DDT. Consequently, the grid resolution of 1×10^{-6} m is considered to be able to describe the DDT process.

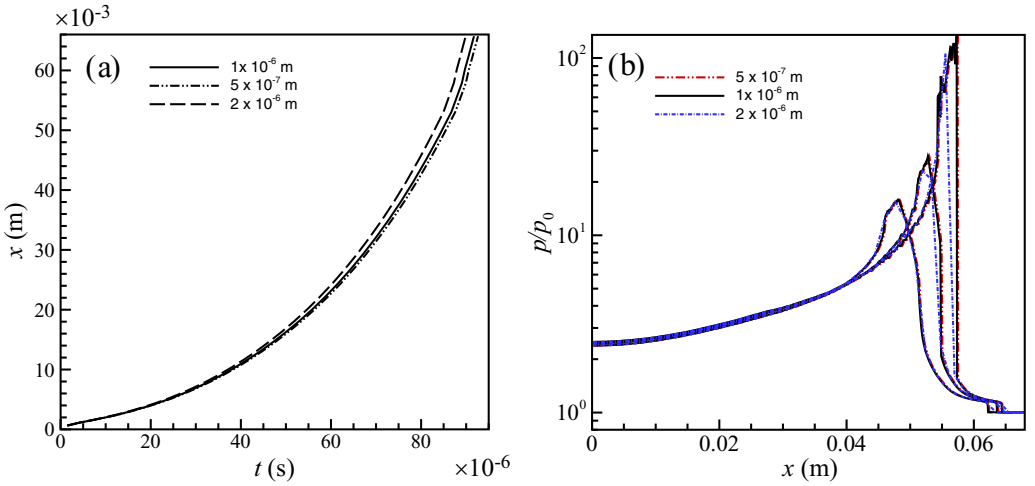

FIG. 15. Verification of grid resolution: (a) x-t plots for three cases; (b) pressure profiles at axis for hot-wall boundary.

We further note that good grid convergence was obtained in the previous works of Wang *et al.* [55]. Dzieminska and Hayashi [49] simulated a DDT in a stoichiometric H_2-O_2 mixture by using a grid resolution of 3×10^{-6} m, while Ivanov *et al.* [56] carried out a three-dimensional (3D) simulation on DDT for H_2-O_2 mixtures at atmospheric pressure and temperature by using a grid resolution of 2.5×10^{-5} m. These prior results further support the present use of the grid resolution of 1×10^{-6} m.

[1] J. H. S. Lee, *The Detonation Phenomenon* (Cambridge University Press, Cambridge, 2008).

[2] V. N. Gamezo, A. M. Khokhlov, and E. S. Oran, The influence of shock bifurcations on shock-flame interactions and DDT, Combust. Flame **126**, 1810 (2001).

[3] M. H. Wu, M. P. Burke, S. F. Son, and R. A. Yetter, Flame acceleration and the transition to detonation of stoichiometric ethylene/oxygen in microscale tubes, Proc. Combust. Inst. **31**, 2429 (2007).

[4] M. A. Liberman, M. Kuznetsov, A. Ivanov, and I. Matsukov, Formation of the preheated zone ahead of a propagation flame and the mechanism underlying the deflagration-to-detonation transition, Phys. Lett. A **373**, 501 (2009).

[5] M. Kuznetsov, V. Alekseev, I. Matsukov, and S. Dorofeev, DDT in a smooth tube filled with a hydrogen-oxygen mixture, Shock Waves **14**, 205 (2005).

[6] S. Kerampran, D. Desbordes, B. Veyssière, and L. Bauwens, Flame propagation in a tube from closed to open end, in *Proceedings of AIAA 39th Aerospace Sciences Meeting and Exhibit* (AIAA, Reston, VA, 2001).

[7] A. M. Khokhlov, E. S. Oran, and G. O. Thomas, Numerical simulation of deflagration-to-detonation transition: the role of shock-flame interactions in turbulent flames, Combust. Flame **117**, 323 (1999).

[8] I. Brailovsky, L. Kagan, and G. Sivashinsky, Combustion waves in hydraulically resisted systems, Philos. Trans. R. Soc., A **370**, 625 (2012).

[9] N. Tsuboi, Y. Morii, and A. K. Hayashi, Two-dimensional numerical simulation on galloping detonation in a narrow channel, Proc. Combust. Inst. **34**, 1999 (2013).

[10] S. B. Dorofeev, M. S. Kuznetsov, and V. I. Alekseev, Evaluation of limits for effective flame acceleration in hydrogen mixtures, J. Loss Prev. Process Ind. **14**, 583 (2001).

[11] M. Kuznetsov, V. Alekseev, Y. Yankin, and S. Dorofeev, Slow and fast deflagrations in hydrocarbon-air mixtures, Combust Sci. Technol. **174**, 157 (2002).

[12] I. Brailovsky, V. Goldshtein, I. Schreiber, and G. I. Sivashinsky, On deflagration-to-detonation transition, Combust. Sci. Technol. **124**, 145 (1997).

[13] D. Valiev, V. Bychkov, V. Akkerman, L.-E. Eriksson, and M. Marklund, Heating of the fuel mixture due to viscous stress ahead of accelerating flames in deflagration-to-detonation transition, Phys. Lett. A **372**, 4850 (2008).

[14] V. Akkerman, V. Bychkov, A. Petchenko, and L.-E. Eriksson, Flame oscillations in tubes with nonslip at the walls, Combust. Flame **145**, 675 (2006).

[15] M. A. Liberman, G. I. Sivashinsky, D. H. Valiev, and L.-E. Eriksson, Numerical simulation of deflagration-to-detonation transition: role of hydrodynamic instability, Int. J. Trans. Phenom. **8**, 253 (2006).

[16] I. Brailovsky and G. Sivashinsky, Hydraulic resistance as a mechanism for deflagration-to detonation transition, Combust. Flame **122**, 492 (2000).

[17] I. Brailovsky and G. Sivashinsky, Momentum loss as a mechanism for deflagration-to detonation transition, Combust. Theory Modell. **2**, 429 (1998).

[18] L. Kagan and G. Sivashinsky, The transition from deflagration to detonation in thin channels, Combust. Flame **134**, 389 (2003).

[19] L. Kagan and G. Sivashinsky, On the transition from deflagration to detonation in narrow tubes, Flow Turbul. Combust. **84**, 423 (2010).

[20] W. H. Han, Y. Gao, and C. K. Law, Flame acceleration and deflagration-to-detonation transition in micro- and macro-channels: An integrated mechanistic study, Combust. Flame **176**, 285 (2017).
[21] C. Wang, Y. Y. Zhao, and W. H. Han, Effect of heat-loss boundary on flame acceleration and deflagration-to-detonation transition in narrow channels, Combust. Sci. Technol. **189**, 1605 (2017).
[22] K. Ishii, K. Itoh, and T. Tsuboi, A study on velocity deficits of detonation waves in narrow gaps, Proc. Combust. Inst. **29**, 2789 (2002).
[23] J. H. S. Lee, Dynamic parameters of gaseous detonations,J. Ann. Rev. Fluid Mech. **16**, 311 (1984).
[24] L. Kagan, On the transition from deflagration to detonation in narrow channels, Math. Modell. Nat. Phenom. **2**, 40 (2007).
[25] Y. Ju and C. K. Law, Propagation and quenching of detonation waves in particle laden mixtures, Combust. Flame **129**, 356 (2002).
[26] J. D. Ott, E. S. Oran, and J. D. Anderson, Jr., A mechanism for flame acceleration in narrow tubes, AIAA J. **41**, 1391 (2003).
[27] J. D. Ott, E. S. Oran, and J. D. Anderson, Jr., The interaction of a flame and its self-induced boundary layer, NASA Report No. CR-1999-209401, 1999 (unpublished).
[28] M. H. Wu and C. Y. Wang, Reaction propagation modes in millimeter-scale tubes for ethylene/oxygen mixtures, Proc. Combust. Inst. **33**, 2287 (2011).
[29] E. S. Oran and V. N. Gamezo, Origins of the deflagration-to detonation transition in gas-phase combustion, Combust. Flame **148**, 4 (2007).
[30] Y. Zeldovich, Regime classification of an exothermic reaction with nonuniform initial conditions, Combust. Flame **39**, 211 (1980).
[31] J. H. S. Lee and I. O. Moen, The mechanism of transition from deflagration to detonation in vapor cloud explosion, Prog. Energy Combust. Sci. **6**, 359 (1980).
[32] M. A. Liberman, M. F. Ivanov, A. D. Kiverin, M. S. Kuznetsov, A. A. Chukalovsky, and T. V. Rakhimova, Deflagration-to-detonation transition in highly reactive combustible mixtures, Acta Astronaut. **67**, 688 (2010).
[33] M. F. Ivanov, A. D. Kiverin, and M. A. Liberman, Hydrogen-oxygen flame acceleration and transition to detonation in channels with no-slip walls for a detailed chemical reaction model, Phys. Rev. E **83**, 056313 (2011).
[34] M. F. Ivanov, A. D. Kiverin, and M. A. Liberman, Flame acceleration and deflagration-to-detonation transition in stoichiometric hydrogen/oxygen in tubes of different diameters, Int. J. Hydrogen Energy **36**, 7714 (2011).
[35] M. A. Liberman, A. D. Kiverin, and M. F. Ivanov, On detonation initiation by a temperature gradient for a detailed chemical reaction models, Phys. Lett. A **375**, 1803 (2011).
[36] M. A. Liberman, A. D. Kiverin, and M. F. Ivanov, Regimes of chemical reaction waves initiated by nonuniform initial conditions for detailed chemical reaction models, Phys. Rev. E **85**, 056312 (2012).
[37] C. Wang, C. G. Qian, J. N. Liu, and M. Liberman, Influence of chemical kinetics on detonation initiating by temperature gradients in methane/air, Combust. Flame **197**, 400 (2018).
[38] R. J. Kee, F. M. Rupley, and J. A. Miller, CHEMKINII: A FORTRAN chemical kinetics package for the analysis of gas phase chemical kinetics, Technical Report No. SAND89-8009B, Sandia National Laboratories, 1992 (unpublished).
[39] R. J. Kee, G. Dixon-Lewis, J. Warnatz, M. E. Coltrin, and J. A. Miller, A FORTRAN computer code package for the evaluation of gas-phase multi-component transport properties, Technical Report No. SAND86-8246, Sandia National Laboratories, 1991 (unpublished).
[40] A. L. Sánchez and F. A. Williams, Recent advances in understanding of flammability characteristics of hydrogen, Prog. Energy Combust. Sci. **41**, 1 (2014).
[41] G. S. Jiang and C. W. Shu, Efficient implementation of weighted ENO schemes, J. Comput. Phys. **126**, 202 (1996).
[42] C. W. Shu and S. Osher, Efficient implementation of essentially non-oscillatory shock-capturing schemes, J. Comput. Phys. **77**, 439 (1988).
[43] C. A. Kennedy and M. H. Carpenter, Additive Runge-Kutta schemes for convection diffusion reaction equations, Appl. Numer. Math. **44**, 139 (2003).

[44] M. P. Burke, M. Chaos, Y. Ju, F. L. Dryer, and S. J. Klippenstein, Comprehensive H_2/O_2 kinetic model for high-pressure combustion, Int J. Chem. Kinet. **44**, 444 (2012).
[45] A. A. Konnov, Remaining uncertainties in the kinetic mechanism of hydrogen combustion, Combust Flame **152**, 507 (2008).
[46] M. Ó. Conaire, H. J. Curran, J. M. Simmie, W. J. Pitz, and C. K. Westbrook, A comprehensive modeling study of hydrogen oxidation, Int. J. Chem. Kinet. **36**, 603 (2004).
[47] C. K. Law, *Combustion Physics* (Cambridge University Press, Cambridge, 2006).
[48] R. W. Houim, A. Ozgen, and E. S. Oran, The role of spontaneous waves in the deflagration-to-detonation transition in submillimeter channels, Combust. Theory Modell. **20**, 1068 (2016).
[49] E. Dzieminska and A. K Hayashi, Auto-ignition and DDT driven by shock wave-boundary layer interaction in oxyhydrogen mixture, Int. J. Hydrogen Energy **38**, 4185 (2013).
[50] B. D. Taylor, D. A. Kessler, V. N. Gamezo, and E. S. Oran, Numerical simulations of hydrogen detonations with detailed chemical kinetics, Proc. Combust. Inst. **34**, 2009 (2013).
[51] V. Bychkov, V. Akkerman, G. Fru, A. Petchenko, and L. E. Eriksson, Flame acceleration in the early stages of burning in tubes, Combust. Flame **150**, 263 (2007).
[52] V. Bychkov, S. Golberg, M. Liberman, and L. E. Eriksson, Propagation of curved stationary flames in tubes, Phys. Rev. E **54**, 3713 (1996).
[53] H. Xiao, R. W. Houim, and E. S. Oran, Effects of pressure waves on the stability of flames propagating in tubes, Proc. Combust. Inst. **36**, 1577 (2017).
[54] B. Xu and Y. Ju, Theoretical and numerical studies of non-equilibrium slip effects on a catalytic surface, Combust. Theory Modell. **10**, 961 (2006).
[55] C. Wang, C. W. Shu, W. H. Han, and J. G. Ning, High resolution WENO simulation of 3D detonation waves, Combust. Flame **160**, 447 (2013).
[56] M. F. Ivanov, A. D. Kiverin, I. S. Yakovenko, and M. A. Liberman, Hydrogen-oxygen flame acceleration and deflagration-to-detonation transition in three-dimensional rectangular channels with no-slip walls, Int. J. Hydrogen Energy **38**, 16427 (2013).